



Stable Rh particles in hydrotalcite-derived catalysts coated on FeCrAlloy foams by electrosynthesis

Patricia Benito^{a,*}, Gert Nuyts^b, Marco Monti^a, Wout De Nolf^b, Giuseppe Fornasari^a, Koen Janssens^b, Erika Scavetta^a, Angelo Vaccari^a

^a Dipartimento di Chimica Industriale "Toso Montanari", Università di Bologna, Viale Risorgimento 4, 40136 Bologna, Italy

^b Department of Chemistry, University of Antwerp, Groenenborgerlaan 171, 2020 Antwerp, Belgium

ARTICLE INFO

Article history:

Received 30 January 2015

Received in revised form 9 May 2015

Accepted 15 May 2015

Available online 19 May 2015

Keywords:

Electrosynthesis

Rh

Rh/Ni

FeCrAlloy

Catalytic partial oxidation of CH₄

ABSTRACT

Rh-based structured catalysts for the Catalytic Partial Oxidation of CH₄ to syngas were prepared by electrosynthesis of Rh/Mg/Al hydrotalcite-type compounds on FeCrAlloy foams and calcination. The effects of Rh content, total metal concentration, and partial replacement of Mg²⁺ by Ni²⁺ in the electrolytic solution on coating thickness, Rh speciation, metallic particle size, and catalytic activity were investigated by SEM/EDS, μ-XRF/XANES and tests under diluted and concentrated reaction conditions.

The amount of Rh species, present as Mg (Rh_xAl_{1-x})₂O₄, depended on the thickness of the electrosynthesised layer as well as the Rh particle size and dispersion. Smaller and more dispersed particles were obtained by decreasing the Rh concentration in the electrolytic solution from Rh/Mg/Al = 11/70/19 to 5/70/25 and 2/70/28 atomic ratio% (a.r.%) and in thinner rather than thicker layers. Despite the improvement in metallic particles features, the CH₄ conversion was negatively affected by the low amount of active sites in the coating, the high metal support interaction and possibly the oxidation of metallic particles and carbon formation.

A larger amount of solid containing well dispersed Rh particles was deposited by increasing the total metal concentration from 0.03 M to 0.06 M with the Rh/Mg/Al = 5/70/25 a.r.%, and the catalytic performances were enhanced. The partial replacement of Mg²⁺ by Ni²⁺ gave rise to a very active bimetallic Rh/Ni catalyst, CH₄ conversion and selectivity to syngas were above 90%, however, it slightly deactivated with time-on-stream.

© 2015 Elsevier B.V. All rights reserved.

1. Introduction

The Catalytic Partial Oxidation (CPO) of CH₄ is nowadays an industrial option to autothermally produce syngas at short contact time values [1]. The CPO catalysts reported in literature are metals (Ni, Co, Pt, Rh) supported on or included in ceramic materials (γ -Al₂O₃, α -Al₂O₃, MgO, MgAl₂O₄, CeO₂ or Ce_{1-x}Zr_xO₂) [2]. Experimental and theoretical studies demonstrated that the catalytic bed is divided in an oxidation and a reforming zone [3–5]. In the short oxidation zone, located at the inlet of the bed, partial and total oxidation products are formed, the temperature largely increases and O₂ consumption is mass transfer limited. In the reforming zone, CH₄ is consumed by Steam Reforming (SR). While water Gas Shift

(WGS) and reverse Water Gas Shift (rWGS) reactions occur along the whole catalytic bed [6].

The high Gas Hourly Space Velocities (GHSV) required to operate at short contact time values increase the heat released by exothermic reactions and the temperature in the catalytic bed. Such high temperatures may promote homogeneous reactions [7], deactivate the catalyst, and lead to safety risks [8,9]. Several efforts have been made to keep the temperature under control, which deal with either the design of the reactor during CPO scale-up [1] or the use of structured catalysts on laboratory scale.

Structured catalysts are made of a three-dimensionally shaped support (i.e. honeycomb, open-cell foam, fibre) coated by a catalytic film [10]. The requirements that a CPO catalyst must meet [2,11] (high CH₄ conversion and selectivity in syngas, stability against sintering, oxidation and carbon formation, fast start-up response) are related to both support and coating features. In particular, they depend on the metal active species and oxide support forming the catalytic film, homogeneity and adherence of the coating, and, last but not least, stability of the 3D support under the harsh reac-

* Corresponding author at: Dipartimento Chimica Industriale "Toso Montanari", ALMA MATER STUDIORUM-Università di Bologna, Viale Risorgimento 4, 40136 Bologna, Italy. Tel.: +39 512093677; fax: +39 512093679.

E-mail address: patricia.benito3@unibo.it (P. Benito).



tion conditions. Hence, the success of a CPO structured catalyst is the result of the chemical formulation of the coating, support morphology and shape, preparation route, and catalyst–3D support interaction.

As materials for the support, honeycombs and open-cell foams made of ceramic (cordierite [12–14], α -Al₂O₃ [3,15,16], SiC [17]) and metallic (Ni [18,19], FeCrAlloy [20–23]) materials are mainly employed.

Under adiabatic conditions the start-up, steady-state and blow-out of the CPO depend on the shape of the support [24,25]. The O₂ mass transfer and, therefore, the heat released by exothermic reactions is controlled by the size and shape of the channels in honeycomb monoliths [26,27]. In non-adiabatic reactors, radiative heat loss helps to decrease hot spots [28,29]. Lastly, the heat transfer by conduction also plays a role in flattening thermal profiles when using thermally conductive supports [17,22].

The lower amount of active catalyst per volume in structured than in pelletized catalysts [10] is usually balanced by depositing a highly active catalyst. Indeed, noble metals, mainly Pt [12,15] and Rh [16,30], are usually the active species; although the use of bimetallic noble metal–nickel or cobalt catalysts [31] and stratified beds [32] are also reported. The amount of active species, which modifies the thermal profile [8,16,26], may be controlled by pore size [33], layer thickness [34], and metal loading [30].

Washcoating or dip-coating [35], or their modifications such as dip-blowing [36], are often adopted to obtain metal supported CPO structured catalysts. The metals are incorporated by impregnation as their respective salts either before [9,14,29] or after [13,16,23] washcoating the ceramic support, as well as directly on the surface of the structured support [12,15,30]. The impregnation on structured supports may give rise to dishomogeneities in metal dispersion. On the contrary, deposition of Pt nanoparticles on α -Al₂O₃ foams by microwave-assisted gel-combustion synthesis in self-propagating mode [37], spontaneous deposition of Rh and Pt particles on Ni foams by metal exchange reactions [19] or electrosynthesis of Rh on FeCrAlloy foams [23] produce small, well-dispersed and distributed metallic particles.

Low surface area supports such as α -Al₂O₃ may lead to large metallic particles with low dispersion [15,16] and metal–support interaction. These features, coupled to the harsh CPO reaction conditions, give rise to changes in the catalyst and, eventually, to its deactivation, depending also on the position within the catalytic bed [15]. In the case of Pt-based catalysts [15,30], metallic species may even be transported from the oxidation to the reforming zone, accompanied by oxidation of Pt⁰ to PtO₂, sintering, and carbon formation. On the other hand, Rh catalysts are more stable [3] and less prone to carbon formation [38]; however, if Rh⁰ particles are not well stabilised, they also suffer from sintering [23]. The oxidation state of Rh during CPO tests is related to operative conditions; at high temperatures (700–1000 °C) Rh is in a reduced state even in the presence of oxygen [39], while at temperatures around 400 °C Rh³⁺ is detected in the oxidation zone [40].

Supports, such as γ -Al₂O₃ [16,33], γ -Al₂O₃ modified by Ce [16], La or P [13,23], AlPO₄ [23], perovskites (LaMnO₃ [17] and LaCoO₃ [31]) improve Rh dispersion and stability. However, special care must be taken during washcoating since the catalyst support may suffer from changes. For instance the wet ball milling step used for the preparation of an AlPO₄ slurry induces pore collapse and decreases the surface area [23].

Hydrotalcite-type (HT) compounds are well-known precursors of catalysts for CPO, since after calcination and reduction small metallic particles are stabilised inside a thermally stable oxide matrix [41]. Hence, it was proposed by some of us to prepare Rh-bulk catalysts coated on FeCrAlloy foams by thermal decomposition of electrosynthesised HT compounds [42–48]. The thermal conductivity of FeCrAlloy is not very high [10]; however, finding a

metallic support able to withstand CPO conditions is not straightforward. The synthesis procedure consists of the precipitation of HT compounds on the surface of the metallic support by an electrogeneration of base method [49]. The reduction of nitrates in aqueous media by application of a cathodic potential produces hydroxyls at the electrode surface, increasing the local pH [46,50]. Despite the electrosynthesis being a promising alternative to the washcoating of HT compounds [51], several aspects need further improvement. Due to the thin film thicknesses obtained in our first experiments, the number of active sites were increased by using electrolytic solutions with a high Rh loading [Rh/Mg/Al = 11/70/19 atomic ratio (a.r.%)]; however Rh particles were quite large (50–200 nm) [48]. Moreover, the coating film was not homogeneous, it was composed by an inner and outer layer, differing in composition. The latter was enriched in cations that precipitate at lower pH, i.e. Al and Rh, indicating an uncontrolled precipitation as the synthesis proceeded. This phenomenon may be ascribed to sequential precipitation of the elements due to an insulating effect of the deposits [45,52], and to mass transfer phenomena [50].

Aim of this paper was to reduce the amount of Rh in the catalytic film without decreasing performances by optimising the Rh particle size, film thickness and active phase composition. Firstly, to decrease the metal particle size and the sintering, the Rh/Mg/Al a.r.% in the electrolytic solution was modified from 11/70/19, used in our previous works [48], to 5/70/25 and 2/70/28. Secondly, to overcome the loss in active sites by lowering the Rh loading, the total metal concentration in the Rh/Mg/Al = 5/70/25 a.r.% electrolytic solution was increased from 0.03 M to 0.06 M and 0.10 M to favour the transport rate of the species towards the working electrode and increase the amount of solid deposited [53,54]. Lastly, to improve the activity, a second active phase, Ni, was added in the coating to form Rh/Ni bimetallic catalysts [55]; the bimetallic Rh/Ni catalyst being prepared by replacing a part of the Mg²⁺ cations by Ni²⁺ ones (Rh/Ni/Mg/Al = 5/15/55/25 a.r.%). The morphology and composition of the samples were analysed by Scanning Electron Microscopy – Energy Dispersive X-ray Spectroscopy (SEM–EDS), and microscopic X-ray Fluorescence (μ XRF). While X-ray Absorption Near Edge Structure (XANES) spectroscopy, measuring the Rh-L₃ line, was used in order to determine the Rh speciation. The catalysts activity was studied by performing CPO tests feeding concentrated and diluted CH₄/O₂/He gas mixtures and operating at the oven temperature of 750 °C.

2. Experimental part

2.1. Synthesis of the catalysts

The electrosyntheses were performed in a single compartment three electrode cell at room temperature, with $1.00 \times 1.19 \text{ cm}^2$ cylinders of FeCrAlloy foam (60 ppi and 4.5% nominal relative density) as Working Electrodes (WE). Prior to the syntheses, cylinders were rinsed with ethanol and water. Electrode potentials were measured with respect to an aqueous Saturated Calomel Electrode (SCE; i.e. Reference Electrode (R.E.)). The Counter Electrode (C.E.) was a Pt gauze (about 18.00 cm^2) placed around the foam cylinder at approx. 0.70 cm. To establish the electrical contact between the foam and the potentiostat, a Pt wire was inserted in the middle of the foam cylinder and other two Pt wires were inserted perpendicular to the previous one in the outer surface of the foam cylinder [48]. Pt wires were well insulated by two layers of teflon tape and parafilm, to avoid their contact with the electrolytic solution and thus ensuring that only the FeCrAlloy acted as working electrode.

The electrochemical syntheses were carried out by chronoamperometry with an Autolab PGSTAT128N (Metrohm) at −1.2 V vs SCE for 2000 s as identified in our previous work [48]. The elec-

trotolytic solutions were aqueous solutions containing the salts of the cations to be precipitated [$\text{Rh}(\text{NO}_3)_3$, $\text{Mg}(\text{NO}_3)_2$, $\text{Al}(\text{NO}_3)_3$ and $\text{Ni}(\text{NO}_3)_2$] with total concentrations of 0.03, 0.06 and 0.10 M. The Rh/Mg/Al a.r.% in the solutions varied from 11/70/19 to 5/70/25 and 2/70/28, while the Rh/Ni/Mg/Al a.r.% was 5/15/55/25. KOH was added to adjust the initial pH of the solutions to 3.8 [44]. After washing and drying at 40 °C, coated foam cylinders were weighed. Samples obtained using the 0.03 M Rh/Mg/Al solution will from now be referred to as RhX-HT, where X refers to the Rh amount (a.r.) i.e. Rh11-HT. The bimetallic sample will be named Rh5Ni-HT, while the samples prepared from the 0.06 M and 0.10 M solutions Rh5-HT-0.06 M and Rh5-HT-0.1 M.

Catalysts were obtained by calcination of coated foams at 900 °C for 12 h (heating rate 10 °C min⁻¹) and will be referred to as Rh11-c900, Rh5-c900, Rh2-c900, Rh5Ni-c900, Rh5-c900-0.06 M and Rh5-c900-0.1 M. The reduced and spent samples will be named by replacing -c900 by -red or -used, respectively, i.e. Rh5-red or Rh5-used.

2.2. Characterisation techniques

SEM/EDS analyses were performed by using an EVO 50 Series Instrument (LEO ZEISS) equipped with an INCAEnergy 350 EDS micro analysis system and INCASmartMap to image the spatial variation of elements in a sample (Oxford Instruments Analytical). An accelerating voltage of 20 kV was applied with a spectra collection time of 60 s; point and area analyses were performed in around 10–15 regions of interest. Secondary and backscattered electron images were collected. Wide regions were spanned to provide a well representative map of the catalysts, namely analyses were performed in tips of the struts, plate zones, and arms connecting plate zones, along the foam cylinder surface. Mg/Rh atomic ratios in the coating were estimated from EDS analyses, using standardless quantification. The contribution of the Al coming from the support makes it difficult to calculate Mg/Al or Rh/Al ratio values in the electrosynthesised solids, thus the amount of Al in the coating was only qualitatively estimated.

FEG-SEM analyses were performed by using a Zeiss LEO Gemini 1530 equipped with an Everhart–Thornley (E-T) secondary electron detector and a Scintillator BSE detector – KE Developments CENTAURUS. The accelerating voltages were 5 or 10 kV. Particle size distributions were obtained by the Image J software, at least 300 particles were analysed.

XANES profiles at the Rh-L₃ edge were collected on beamline ID21 at the European Synchrotron Radiation Facility (ESRF, Grenoble F) [56]. The storage ring operating conditions were 6 GeV electron energy with 200 mA electron current and 7/8 multibunch operating mode. For these experiments a Si (111) double-crystal monochromator was used, having an energy resolution of $10^{-4}(\Delta E/E)$.

A metallic Rh reference foil (0.75 μm) was used to provide an accurate energy calibration for all the spectra (first inflection point of the Rh-L₃ edge set at 3004.0 eV [57]). For all XANES measurements, reference compounds and actual catalysts spectra were recorded with the sample positioned at 62° with respect to the incoming beam. The fluorescence was recorded as a function of the incident X-ray energy at an angle of 49° with respect to the sample. XANES spectra were collected from ~35 eV below to ~130 eV above the Rh-L₃ edge (2970 eV–3135 eV), with 0.25 eV steps for the entire measured region. A 100 ms integration time was used for each energy resulting in a measuring time of ~1 min per XANES spectrum. 20–30 repeats were recorded to acquire noise-free spectra.

To obtain reference spectra, appropriate amounts of Rh model compounds were mixed with boron nitride, resulting in a weight percentage of 2 of the model compound to limit self-absorption.

Each mixture was compressed into a pellet and placed in a sample holder. To avoid contributions of possible heterogeneities during mixing, measurements were performed with an unfocused beam using a 200 μm pinhole. Where needed (low Rh content in pellet) no pinhole was used resulting in a beam size of ~500 μm². The fluorescence was recorded using a photodiode or a silicon drift diode (Bruker) (depending on the count rate).

For the measurements of the actual catalysts the beam size was reduced to 0.22 × 0.85 μm² by using zone plate optics. Foam cylinders were embedded in a resin (Technovit 4006, Heraus Kulzer, Germany) and cut; finally polished cross-sections of the struts were analysed. The thickness of the embedded samples prevented transmission measurements thus allowing only monitoring of the fluorescence intensity as a function of the excitation energy. For this purpose a silicon drift diode was used. Prior to XANES measurements, μXRF maps were collected using the same setup and detector previously described with a step size of down to 0.5 μm. A primary excitation energy of 3008 eV was employed in order to obtain a good XRF intensity for Rh present in the layer. These maps were used to locate interesting spots inside the Rh layer at which XANES spectra were recorded. In all maps a measuring time of 100 ms per pixel was used.

For all the XANES spectra, the normalization was performed by means of the software package ATHENA [58]. An edge-step normalization was performed by linear pre-edge subtraction and by regression of a (in general) quadratic polynomial beyond the edge [58]. If a silicon drift detector was used for the collection of XANES spectra, the recorded XRF spectra were evaluated using the PyMCA software package [59]. The fitted Rh intensity (sum of all Rh-L lines) was then plotted as a function of the excitation energy resulting in a (fluorescence mode) XANES spectrum. Analysis was performed by linear combination fitting of unknown spectra with spectra of known Rh reference compounds.

2.3. Catalytic tests

A quartz reactor (i.d. 10.0 mm) was placed in an electrical oven and it was loaded with two foam cylinders, which were located in the isothermal zone of the oven. The foam cylinders were made to fit well with the diameter of the reactor in order to minimize any by-pass phenomena. In situ reduction was performed by feeding an equimolar H_2/N_2 mixture (7.0 L h⁻¹) for 2 h at 750 °C prior to catalytic tests. The temperature at the inlet of the bed was monitored by a chromel alumel thermocouple placed inside a quartz wire. Reactant gases were supplied from individual cylinders and gas flow rates were measured with mass flow controllers, being mixed before entering in the quartz reactor. GHSV values and the composition of the gas mixture were varied as follow: GHSV = 11,500, 15,250, 38,700 and 63,300 h⁻¹ (calculated on the total volume of the foam support at STP conditions) and $\text{CH}_4/\text{O}_2/\text{He}$ = 2/1/20 or 2/1/4 v/v. Reaction products were analysed on-line, after water condensation, by a PerkinElmer Autosystem XL gas chromatograph, equipped with two thermal conductivity detectors (TCD) and two Carbosphere columns using He as carrier gas for CH_4 , O_2 , CO, and CO_2 analyses, and N_2 for the H_2 analysis. CH_4 conversion and the selectivity in H_2 and CO were calculated according to the previously reported formulas [60]. Oxygen conversion was completed in all the experiments.

3. Results and discussion

3.1. Effect of Rh content

3.1.1. SEM/EDS analyses

Selected SEM images taken across samples after electrosyntheses with the three different solutions, Rh/Mg/Al = 11/70/19,

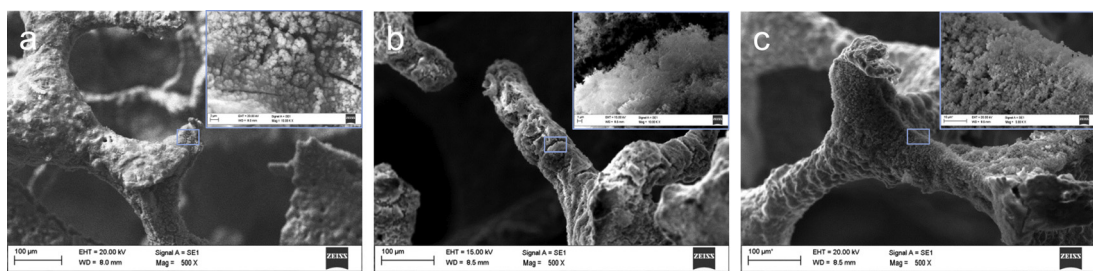


Fig. 1. Secondary SEM images of samples prepared at -1.2 V for 2000 s with different electrolytic solutions: (a) Rh11-HT:Rh/Mg/Al = 11/70/19 a.r.%; (b) Rh5-HT:Rh/Mg/Al = 5/70/25 a.r.%; (c) Rh2-HT:Rh/Mg/Al = 2/70/28 a.r.%.

5/70/25 and 2/70/28 a.r.%, are displayed in Fig. 1. The composition of the electrolytic solution does not alter the typical features of electrosynthesised materials [48]. The foam surface is almost entirely covered by a solid constituted of spherical nanoparticles and platelets, only some uncoated struts are identified. Preferential precipitation occurs on the tips resulting in a 5–15 μm film, and potassium deposits together with the expected elements.

When a thin film is deposited (2–6 μm), the Rh/Mg/Al a.r.% in the coating and the electrolytic solution is quite similar for all samples (Table 1). For thicker films the concentration of Rh and Al in the solid increases as the synthesis proceeds, forming an outer layer with different composition. Namely the sequential precipitation of layers of different composition, previously observed for Rh11-HT [48], also occurs in Rh5-HT and Rh2-HT samples; although next to these similarities some differences among samples are found in film thickness and composition. The Rh content in the outer film depends on its concentration in the electrolytic solution (Table 1), the higher the Rh concentration in the solution, the higher the Rh content in the solid; moreover, it seems that the outer layer is not as abundant in Rh2-HT as in Rh11-HT. The preferential precipitation of Al and Rh may be due to a decrease of the pH in the vicinity of the support when thick films deposit, due to an increase of the electrical resistance in the solid and/or to a mass transfer limiting step of the electroactive species to the metallic foam surface.

The thickness, compactness, and chemical composition of the precursor film determine the properties of the catalytic coating after calcination at $900\text{ }^\circ\text{C}$ for 12 h. SEM images of calcined coated foams are displayed in Fig. 2. Likewise for Rh11-c900 sample [48], the Al-rich layers identified in electrosynthesised Rh5-HT and Rh2-HT samples develop a high number of cracks and the solid easily detaches. In some cases it is possible to observe alumina needles, coming from either the oxidation of the foam or the electrodeposited film. On the other hand, Mg-rich coatings or those whose composition is closer to the expected one are better adhered and more stable after calcination at high temperature. These catalytic coatings are constituted by flakes of globular or platelet-shaped nanoparticles; although some struts are crack free. As for Rh, its concentration in the catalytic layer measured by EDS correlates to the amount of Rh in the solution: Rh11-c900: 10–30 wt.% > Rh5-c900: 5–15 wt.% > Rh2-c900: 1–5 wt.%.

The above commented features of calcined samples may be explained considering that the composition of the precipitated

Table 2

Summary of the average film thicknesses obtained for the Rh/Mg/Al = 11/70/19 a.r.% struts at the different stages in the life cycle. The mean value is given as an indication for the average thickness of the Rh layer while the standard deviation is given as an indication for the variation of the thickness.

	Rh FWHM (μm)	Stdev	Mg FWHM (μm)	Stdev
R11-HT	4.9	1.9	3.9	1.6
R11-c900	4.2	1.2	4.1	1.6
R11-red	9.3	3.6	7.5	3.3
R11-used	6.7	2.6	5.0	1.9

film determines the thermal decomposition of the hydroxides and thermal-expansion coefficients of the formed oxides [61], as well as the chemical interaction between elements of the coating and metallic support, such as previously reported for electrosynthesised catalysts [47]. For instance, high amounts of Mg may favour the solid-state reaction between Al from the foam and Mg from the coating, increasing the stability of the film; although the formation of the protective Al_2O_3 scale may be decreased.

3.1.2. μ XRF/XANES measurements

μ XRF/XANES measurements were performed on cross-sections of selected embedded foams to characterise Rh species. To obtain representative results several regions were analysed, namely coated struts in the top, middle and bottom of foam cylinders. Selected representative data for the sample prepared with the Rh/Mg/Al = 11/70/19 a.r.% solution at the different steps of the life cycle are displayed in Figs. 3 and 4.

XRF maps (Fig. 3) were recorded at 0.5 μm resolution of sectioned struts to select the points to be analysed by XANES (Fig. 4). The Fe-L distribution maps were used to represent the foam support, the Cr-L distribution is rather similar and thus not shown. To give information about the coating composition Mg-K, Al-K and Rh-L distribution maps are shown.

An estimation of each film thickness was obtained by fitting a gaussian to several Mg-K and Rh-L line profiles across the film (Figs. S1, S2, S3, and S4, Supplementary information). The FWHM of these gaussians are given in Table 2; the mean value is an indication for the average layer thickness while its standard deviation is an indication for the variation in thickness.

Elemental distribution maps of cross-sections for Rh11-HT (see as an example Fig. 3A) indicate that Mg, Rh and Al follow a similar distribution in regions of interest located in different areas of

Table 1

Nominal Rh/Mg/Al a.r.% in the electrolytic solutions and estimation of the Rh/Mg/Al a.r.% in the coating by SEM-EDS analysis for the three compositions. Results correspond to the inspection of 10–15 regions of interest.

Atomic ratio%	Rh11-HT			Rh5-HT			Rh2-HT		
	Rh	Mg	Al	Rh	Mg	Al	Rh	Mg	Al
Electrolytic solution	11	70	19	5	70	25	2	70	28
Thin film	2–15	70–85	13–23	3	75	22	2	75	23
Outer film	30	10	60	15	20	65	6	13	81

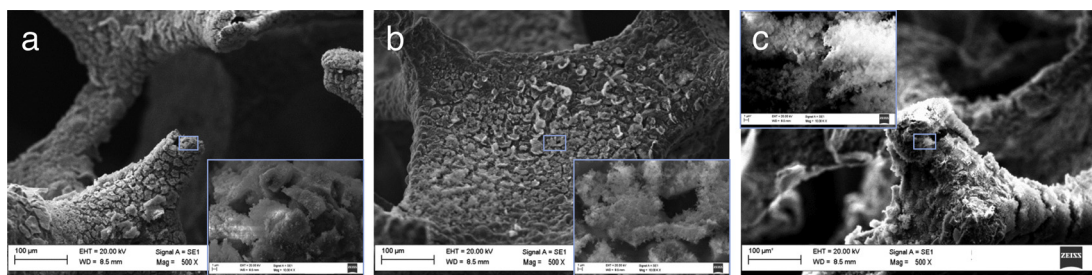


Fig. 2. Secondary SEM images of samples after calcination at 900 °C for 12 h. Rh11-c900 (a), Rh5-c900 (b), Rh2-c900 (c).

the foam surface. On the other hand, the film thickness depends on the inspected region; thicknesses range from 2 to 10 μm with an average value of around 5 μm for Rh and 4 μm for Mg in the selected area displayed in Fig. 3. The thicker Rh than Mg layer may be explained considering that the outer layer mainly contains Rh and Al as previously observed by SEM/EDS. High resolution XRF maps of hollow struts once again confirm that the electrosynthesis takes place in both the outer and inner surface, increasing the surface available for catalytic tests [47]. Selected regions, corresponding to several concentrations of Rh in the layer, were examined by XANES (Table S1, Supplementary information). Rh-L₃ XANES spectra (Fig. 4, point B1) display a white-line at 3007.0 eV due to the electron transition from 2p_{3/2} to 4d_{3/2} and 4d_{5/2}, the peaks at higher energies are attributed to transitions to pd, df, f and df orbitals [62]. LCF reveals that, regardless of the inspected region, Rh is present in a spinel structure forming a Mg (Rh_xAl_{1-x})₂O₄ solid solution rather than segregated as Rh₂O₃, which was detected in samples prepared by electrosynthesis using KNO₃ as supporting electrolyte [47].

After calcination (Fig. 3B) the correlation between the distribution of Rh, Mg and Al remains; however, Rh and Mg coating thicknesses are similar, around 4 μm (Table 2). The interdiffusion

of the species or the detachment of the outer layer during calcination may explain this behaviour. XRF maps of hollow struts once again confirm that the electrosynthesis takes place in both the outer and inner surface, increasing the surface available for catalytic tests [47]. Selected regions, corresponding to several concentrations of Rh in the layer, were examined by XANES (Table S1, Supplementary information). Rh-L₃ XANES spectra (Fig. 4, point B1) display a white-line at 3007.0 eV due to the electron transition from 2p_{3/2} to 4d_{3/2} and 4d_{5/2}, the peaks at higher energies are attributed to transitions to pd, df, f and df orbitals [62]. LCF reveals that, regardless of the inspected region, Rh is present in a spinel structure forming a Mg (Rh_xAl_{1-x})₂O₄ solid solution rather than segregated as Rh₂O₃, which was detected in samples prepared by electrosynthesis using KNO₃ as supporting electrolyte [47].

By decreasing the Rh loading in Rh5-c900 and Rh2-c900 samples (Table S2, Supplementary information), the elemental distributions and Rh speciation remain similar to those in Rh11-c900. Rh, Mg

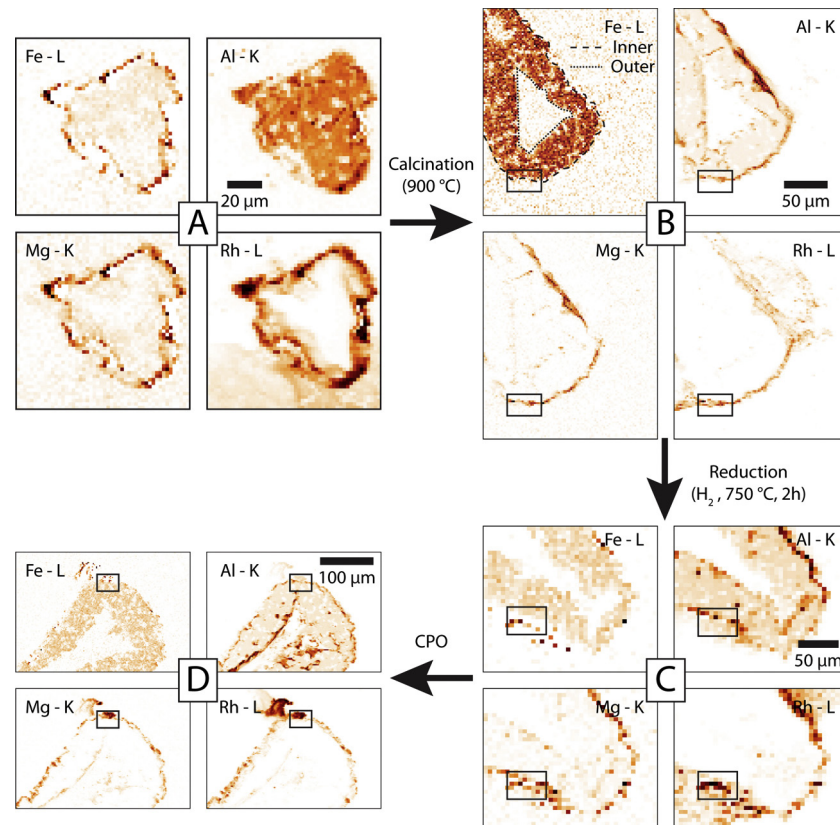


Fig. 3. Elemental distribution maps recorded on cross-sections of a structured Rh catalyst (Rh/Mg/Al = 11/70/19 a.r.%) at different stages in the life cycle. (A) After electrochemical deposition of Rh³⁺, Al³⁺ and Mg²⁺ ($100 \times 100 \mu\text{m}^2$). (B) After calcination of the precursor at 900 °C ($200 \times 236 \mu\text{m}^2$). (C) After reduction under H₂ flow ($215 \times 175 \mu\text{m}^2$). (D) After use in the catalytic partial oxidation of CH₄ reactor ($326 \times 222 \mu\text{m}^2$). On the Fe-L distribution map (B), the inner and outer surface are marked and the black rectangles indicate regions wherein more detailed maps were recorded.

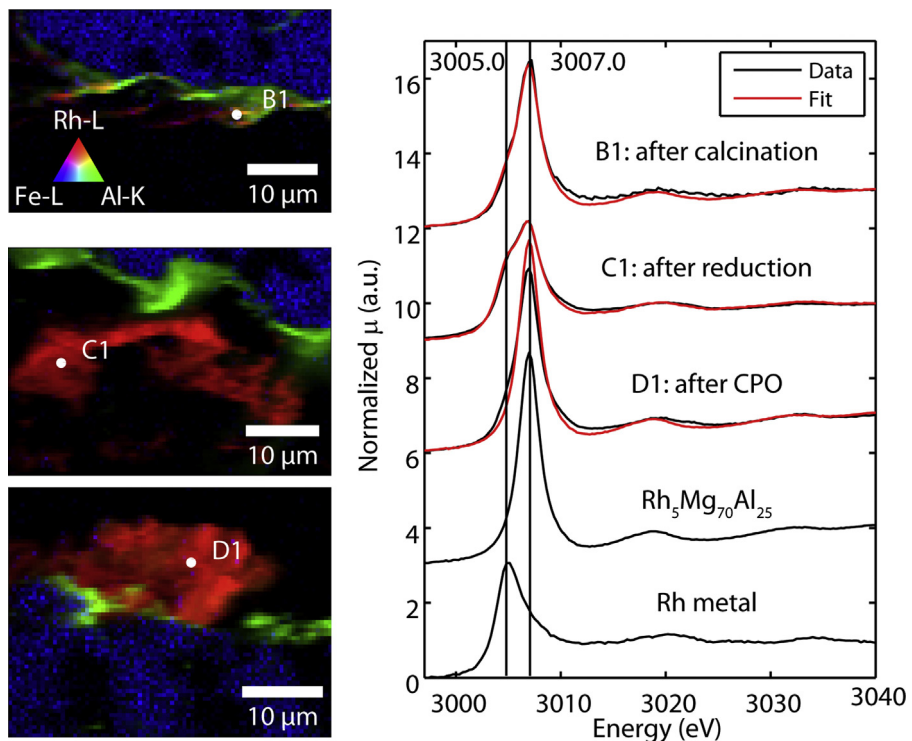


Fig. 4. RGB composite maps (details of the maps shown in Fig. 3) of cross-sections of $\text{Rh}/\text{Mg}/\text{Al} = 11/70/19$ a.r.% struts after calcination (4b), after reduction (4c) and after CPO (4d). The given numbers mark the spots where XANES measurements were performed; an example of the result of a linear combination fit is given for each state. The typical white-line energies for metallic Rh (3005.0 eV) and Rh in a spinel (3007.0 eV) are given.

and Al cover the foam surface, and Rh^{3+} species are included in the MgAl_2O_4 spinel.

The formation of the Mg ($\text{Rh}_{x}\text{Al}_{1-x}\text{O}_4$) solid solution may prevent the sintering of Rh^0 particles; however the Rh^{3+} to Rh^0 reducibility decreases [47], since higher temperatures are required to perform the reduction. In order to obtain information about the reducibility of Rh, the sample with the highest Rh loading was studied after the reduction treatment before catalytic tests, Rh11-red (Figs. 3C and 4c point C1). A less intense white-line at 3005.0 eV due to the decrease of 4d holes is expected for the reduced sample [63,64]. However, the white-line of Rh11-red sample is composed of two overlapped peaks at 3005.0 and 3007.0 eV (Fig. 4, point C1) due to the presence of both Rh^0 and Rh^{3+} species in the coating. The amount of Rh^0 species varies from 21 to 54% in the analysed points. Hence, the Rh^{3+} reduction is incomplete during the activation treatment in H_2 , although the oxidation of the metallic particles during the preparation of the samples may not be discarded.

3.1.3. Catalytic activity

Catalytic tests were performed feeding two $\text{CH}_4/\text{O}_2/\text{He}$ mixtures (2/1/20 and 2/1/4 v/v) to the reactor, with the following GHSV values: 63,300, 38,700, 15,250, and 11,500 h^{-1} . Initial reaction conditions, namely $\text{CH}_4/\text{O}_2/\text{He} = 2/1/20$ v/v and 63,300 h^{-1} , were set also at the end of every test condition to evaluate a possible deactivation/activation of the catalysts (control test). The evolution of CH_4 conversion and selectivity in CO and H_2 with time-on-stream (TOS), by modifying the reaction conditions, for the three catalysts are summarised in Figs. 5 and 6.

In the case of Rh11-c900, feeding the diluted reaction gas mixture at 63,300 h^{-1} , the CH_4 conversion is around 82% during the first 120 min of TOS. Conversely, Rh5-c900 and Rh2-c900 catalysts activated with TOS and the CH_4 conversion value is related to the Rh content within the coating layer. After 120 min of TOS, the conversion value increases from 70 to 76% for Rh5-c900 and from 55 to

60% for Rh2-c900. The main reaction products with Rh11-c900 and Rh5-c900 catalysts are CO and H_2 , although the syngas selectivity is lower for the latter catalyst. On the other hand, the Rh2-c900 sample shows a higher selectivity in CO than in H_2 at the beginning of tests, the differences being smoothed with TOS.

Catalytic performances improve as the GHSV values decrease to 38,700 and 15,250 h^{-1} , in agreement with the behaviour previously reported by some of us for this type of catalysts [44,45]. Quite stable performances are achieved with the Rh11-c900 catalyst, regardless of the total flow rate, with a conversion above 90% at 15,250 h^{-1} . On the contrary, Rh5-c900 and Rh2-c900 samples slightly deactivate with TOS (ca. 1% loss in CH_4 conversion); the former only at 15,250 h^{-1} , while the latter both at 38,700 and 15,250 h^{-1} .

Control tests evidenced that runs at 38,700 h^{-1} and 15,250 h^{-1} do not largely modify the Rh11-c900 and Rh5-c900 catalysts; nevertheless the Rh2-c900 sample shows increased conversion and selectivity values after both catalytic tests.

To explain the catalytic behaviours (namely, activation with TOS, activity and stability of the catalysts) the properties of the coating, i.e. thickness and composition, and the reactions taking place in the catalytic bed have to be considered. CH_4 is converted by the exothermic total or partial oxidation reactions, and by the endothermic SR. On the whole, in diluted reaction conditions, the higher the Rh loading and coating thickness, the better the performances are. Considering that oxidation reactions are fast and controlled by O_2 mass-transfer [27], the differences in conversion and selectivity may be related to the ability of the catalyst to perform the consecutive SR reaction. A small amount of exposed Rh^0 active sites due to low Rh loading in the coating, the formation of large particles or the presence of unreduced Rh^{3+} species, may decrease the CH_4 conversion by SR. For instance, in Rh5-c900 and Rh2-c900 catalysts, the activation observed with TOS suggests that the presence of some hardly reducible Rh^{3+} species decreases their initial activity, while the reaction conditions may help to reduce

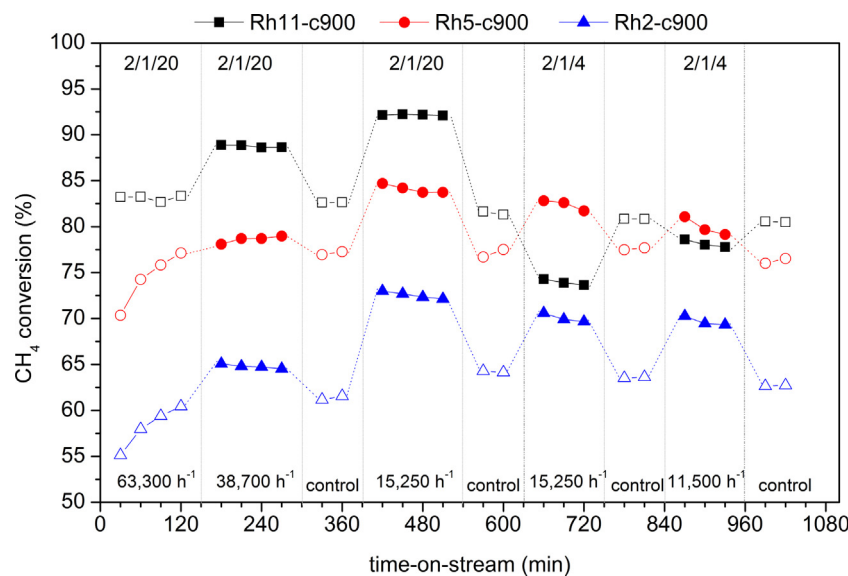


Fig. 5. Evolution of CH_4 conversion with time-on-stream obtained with catalysts synthesised using different electrolytic solutions: Rh11-c900, Rh5-c900 and Rh2-c900. $T_{\text{oven}} = 750^\circ\text{C}$, $\text{CH}_4/\text{O}_2/\text{He} = 2/1/20$ and $2/1/4$ v/v, GHSV = 63,300, 38,700, 15,250, and $11,500 \text{ h}^{-1}$.

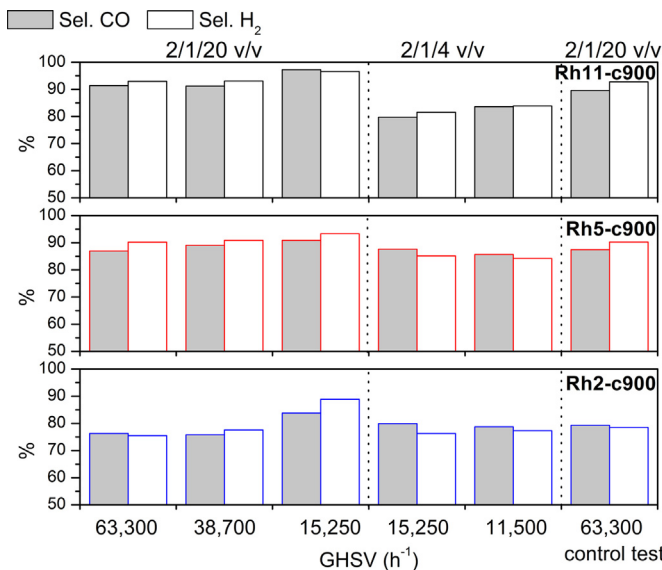


Fig. 6. Average selectivities in CO and H_2 obtained with catalysts synthesised using different electrolytic solutions: Rh11-c900, Rh5-c900 and Rh2-c900. $T_{\text{oven}} = 750^\circ\text{C}$, $\text{CH}_4/\text{O}_2/\text{He} = 2/1/20$ and $2/1/4$ v/v, GHSV = 63,300, 38,700, 15,250, and $11,500 \text{ h}^{-1}$.

some of them and enhance the performances. On the other hand, it should be considered that the SR produces a large amount of H_2 , thus if its contribution lowers, not only the CH_4 conversion, but also the selectivity in H_2 decreases, as observed for the Rh2-c900 sample. At lower GHSV values, the improvement in the conversion is related to the lower CH_4 flow, while the contribution of the heat generated may explain the differences in stability. The heat developed by exothermic reactions contributes to the catalytic activity and it depends on the total flow rate. In tests at $38,700 \text{ h}^{-1}$ and $15,250 \text{ h}^{-1}$ it is reduced, hence it will not help to keep the catalysts active with TOS.

Feeding more concentrated gas mixtures the trend of conversion and selectivity values changes. The most active and selective catalyst is Rh5-c900; the largest differences with Rh2-c900 and Rh11-c900 samples are observed at $15,250 \text{ h}^{-1}$. The temperature increase due to exothermic oxidation reactions is higher in tests with concentrated gas mixtures; however, the amount of CH_4 to

be converted and the partial pressure of the reactants are higher, having an effect on both conversion and stability. The temperature increase promotes the catalytic activity, however it also favours the sintering of metallic particles. It is noteworthy that all the catalysts, regardless of their composition, lose activity with TOS, around 2% in CH_4 conversion, as confirmed by the control test. However, it appears that the deactivation is partially reversible, namely the catalyst steadily recovered the original activity with TOS under the control test. Since the sintering is not reversible, but the oxidation is, the latter phenomenon may explain the loss of activity; although the gasification of some deposited carbon cannot be excluded.

3.1.4. Characterisation of spent samples

The coating is modified during catalytic tests due to the gas flow rate and the temperatures inside the catalytic bed. A general behaviour is observed for all three catalysts, which is related to the composition and morphology of the fresh catalysts [48]. Selected SEM images of the Rh5-c900 catalyst cylinders placed at the inlet of the catalytic bed are displayed in Fig. 7 as an example. Partial detachment occurs in the outer film enriched in Al and Rh (Fig. 7a), and mostly in the foam cylinder placed at the inlet of the catalytic bed. On the contrary, the film in close contact with the foam surface, formed by plate-like or globular particles remains well adhered. Whenever the amount of cracks increases the characteristic Al_2O_3 needles, previously identified in some calcined samples, are observed; although it would appear that they are more abundant in the spent samples. This behaviour may be explained considering that in the sample before catalytic tests some of the needles may be coated by the catalyst layer so it was not possible to identify them, or that during catalytic tests the formation of Al_2O_3 scale continued.

Carbon on the catalyst surface was detected by EDS, mainly in the foam cylinder placed at the outlet of the catalytic bed, in agreement with previous studies that revealed that the absence of gas-phase O_2 favours the formation of carbonaceous deposits [15]. High resolution FEG-SEM images confirm that both patches (Fig. 7b) and nanotubes of carbon (ca. 50 nm diameter) (Fig. 7c) are formed on the catalyst surface.

The Rh particle size distributions were studied by FEG-SEM backscattering images. In Fig. 8 are shown the images of the outer layers of spent catalysts at different Rh loadings, taken from the

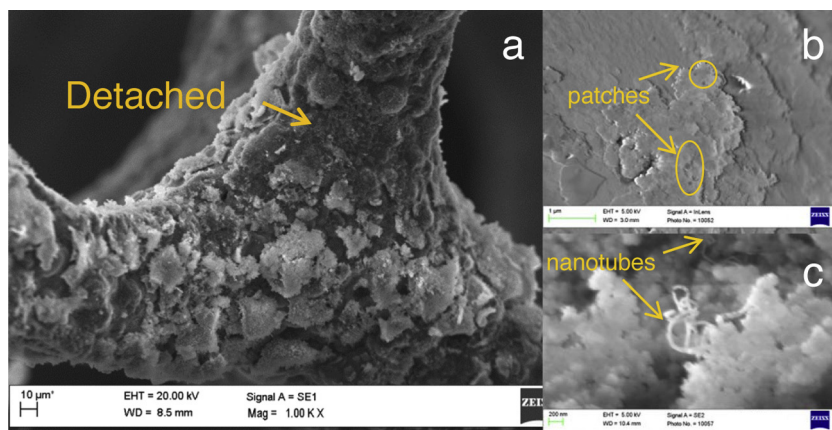


Fig. 7. Secondary SEM (a) and FEG-SEM (b, c) images of the surface of the Rh5-used cylinder placed at the inlet of the catalytic bed. (a) Detail of a detached solid; (b) patches of carbon; (c) carbon nanotubes.

cylinders placed at the top of the catalytic bed, and the particle size distributions obtained by analysing representative regions of interest. A broad particle size distribution (20–200 nm) is measured in Rh11-used sample (Fig. 8a and a*). The frequency of particles in the 20–100 nm range increases for Rh5-used sample (Fig. 8b and b*), although some irregular shaped and large agglomerates of particles are still found. Regarding the inspection of films of different thickness, for both Rh5-used and Rh11-used catalysts, the largest metallic particles are predominantly located in the thickest layers, while smaller and more dispersed particles are observed in thin layers corresponding to Mg-rich coatings and in the middle of needles and plates. The particle size largely decreases for Rh2-c900 spent sample (Fig. 8c and c*); a narrow particle size distribution in the 4–40 nm range is measured, even in some regions where the Rh wt.% was high. Hence, the Rh content in the film, which is related to the concentration of Rh in the electrolytic solution and the film thickness, determines the Rh particle size distribution.

For Rh11 used samples the two foam cylinders loaded in the catalytic reactor were analysed by μ XRF/XANES. In agreement with SEM/EDS characterisation, Rh, Mg and Al elemental distribution maps indicate that the film in close contact with the foam surface is well adhered (Fig. 3D). The measured thickness is comparable to

the calcined sample, although there are some points wherein the Rh thickness is larger than the Mg thickness (Table 2 and Fig. S4). The white-line in XANES spectra (Fig. 4, point D1) is composed of the two overlapped peaks already identified in the reduced sample, due to the coexistence of both Rh^0 and Rh^{3+} in used samples. LCF (Table S1, Supplementary information) reveals that the amount of Rh^0 is lower in the foam placed at the inlet (10–35% of Rh^0) than at the outlet of the catalytic bed (ca. 40% of Rh^0), these values differ from those obtained for the Rh11-red sample (21–54% Rh^0). It is noteworthy that all the measurements were performed ex-situ, therefore as previously commented for the Rh11-red sample, the oxidation of Rh^0 by exposure to the air cannot be discarded. However, the shutdown of the reactor was performed as in ref [39], shutting CH_4 and O_2 simultaneously, thus avoiding modifications in the catalyst. From our results it appears that, despite the high temperatures reached in the catalytic bed, some Rh^{3+} species are still present. The oxidation of CH_4 is a fast reaction and the consumption rate of O_2 is mass transfer limited [27]. However, the CH_4 molecule firstly has to be activated by the metallic particles. Hence, if the number of active sites is not large enough to activate CH_4 , as in some of these structured catalysts, O_2 may foster the Rh^0 oxidation.

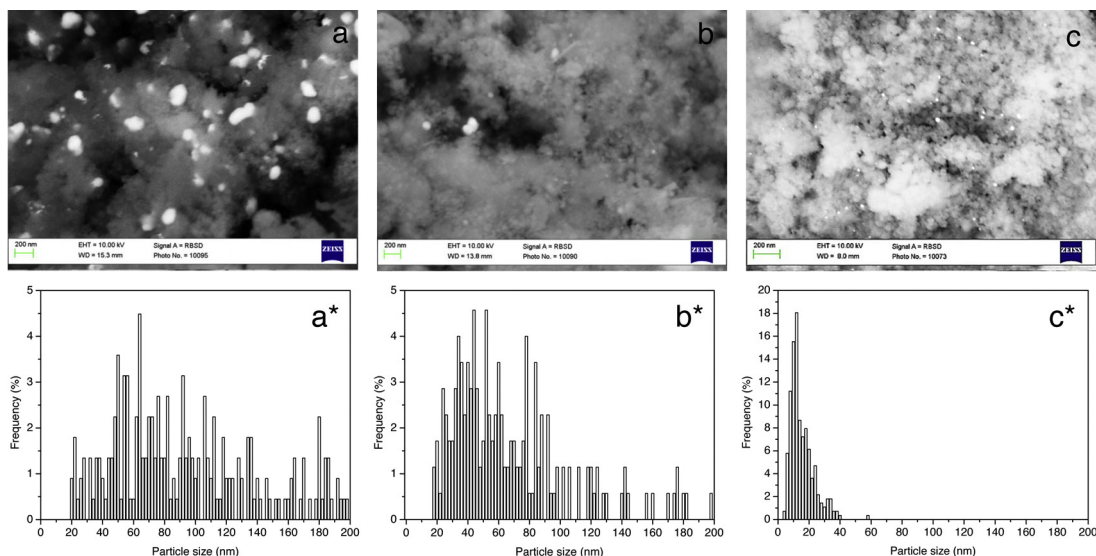


Fig. 8. Rh particles (a–c) and particle size distribution (a*–c*) identified in backscattering FEG-SEM images of the spent catalyst cylinders placed at the inlet of the bed and prepared with electrolytic solutions at different Rh/Mg/Al a.r.%. Rh11-used (a, a*); Rh5-used (b, b*); Rh2-used (c, c*).

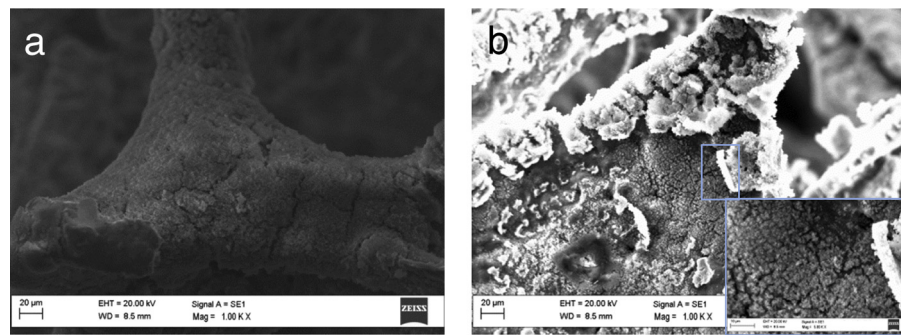


Fig. 9. Secondary SEM images of samples obtained after electrosynthesis at -1.2 V for 2000 s with a $\text{Rh}/\text{Mg}/\text{Al} = 5/70/25$ a.r.% and total metal concentration of 0.06 M, Rh5-HT-0.06 M (a), and after calcination at 900°C for 12 h, Rh5-c900-0.06 M (b).

In summary, the size of the metallic particles is reduced by decreasing the concentration of Rh species in the electrolytic solution. However the lower amount of active sites is responsible of a lower catalytic activity and the composition of the solid is not controlled yet.

3.2. Effect of total Rh/Mg/Al concentration

In the electrosynthesis a limiting step to achieve the desired composition and thickness may be the mass transfer from the bulk of the solution to the vicinity of the support [65], as observed in the reduction of nitrate [50]. To enhance the nitrate and cation mass transfer, the total concentration of Rh, Mg and Al nitrates was increased from 0.03 M to 0.06 M and 0.10 M, while the Rh/Mg/Al ratio was kept constant at 5/70/25 a.r.%. Due to the higher concentration of electroactive nitrates a higher cathodic current was measured (results not shown). Considering that only faradaic current flows through the system, it may be stated that a larger amount of nitrates is reduced generating a higher amount of hydroxyl species; however, the contribution of H_2O electrolysis and O_2 reduction to the increase of pH may not be discarded [48,50,66].

As a result of the above commented effects and taking into account the key role of the pH in the deposition of this type of materials [46], an increase in the amount of deposited solid and in the coating homogeneity are obtained with the 0.06 M

solution (Fig. 9a). The shape of the individual particles, globular and platelets, is not largely altered although they seem to be slightly smaller than in previous samples, leading to a more compact film with less cracks, probably on account of a higher supersaturation. Film thicknesses are around 15–20 μm in the most exposed areas, while in plate zones they are around 5 μm . As for the composition, a.r. values close to the expected one ($\text{Rh}/\text{Mg}/\text{Al} = 4/68/28$ a.r.%) are measured in some parts of the foam. On the other hand, when thicker layers are observed, the sequential precipitation still takes place ($\text{Rh}/\text{Mg}/\text{Al} = 10/39/51$ and 14/26/60 a.r.%).

A further increase in the cation concentration to 0.10 M has a negative effect on the coating properties (results not shown). A large amount of solid precipitates, forming some crusts; however, it easily detaches and the deposition is not controlled as previously observed for $\text{Mg}(\text{OH})_2$ coatings [54]. Not only the composition of the solid differs from the expected one, but also the formation of Rh^0 particles takes place with the 0.10 M solution.

The enhanced coverage in the precursor in terms of thickness and homogeneity obtained with the 0.06 M instead of the 0.03 M solution, leads to an improvement in the film features of the calcined sample. However, it is not possible to completely avoid the formation of cracks related to differences in thermal expansion coefficients and film shrinkage, consequently the detachment of the outer layer occurs (Fig. 9b). An average Rh concentration of 5–15 wt.% is measured by EDS analyses.

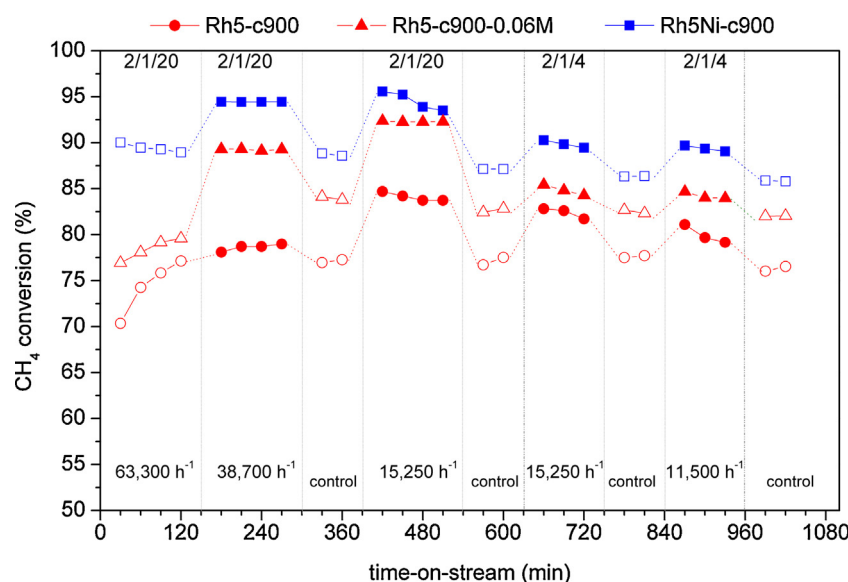


Fig. 10. Evolution of CH_4 conversion with time-on-stream obtained with catalysts synthesised using the 5/70/25 a.r.% electrolytic solution and different total metal concentration, 0.03 M (Rh5-c900) and 0.06 M (Rh5-c900-0.06 M) and with the bimetallic catalyst, Rh5Ni-c900: 5/15/55/25 a.r.%. $T_{\text{oven}} = 750^\circ\text{C}$, $\text{CH}_4/\text{O}_2/\text{He} = 2/1/20$ and 2/1/4 v/v, GHSV = 63,300, 38,700, 15,250, and 11,500 h^{-1} .

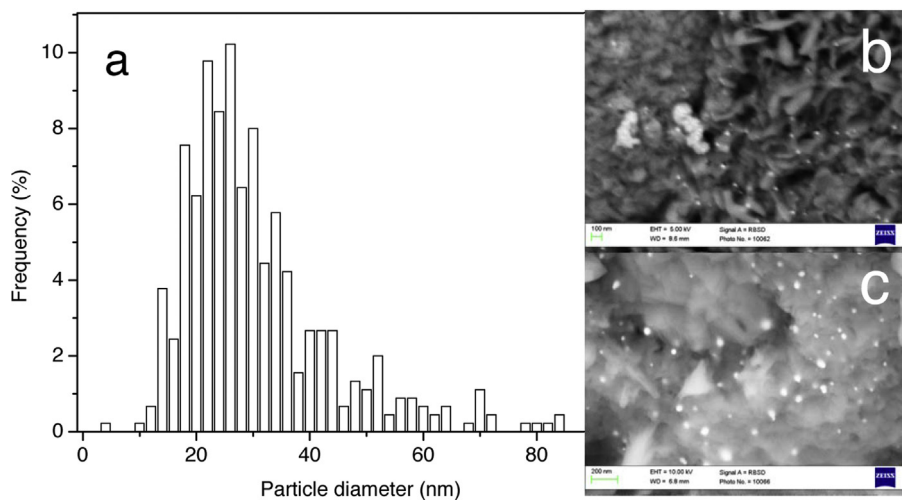


Fig. 11. Secondary SEM: (a) and FEG-SEM, (b, c) images of Rh5-used-0.06 M sample placed at the inlet of the catalytic bed.

A comparison between CH₄ conversion values obtained with catalysts prepared with 0.06 M and 0.03 M solutions is summarised in Fig. 10. The values in conversion of CH₄ and syngas selectivity (not shown) achieved with the Rh5-c900-0.06 M catalyst overcome those of the Rh5-c900 sample in all the reaction conditions investigated. In contrast, the catalyst stability with TOS is only improved during diluted tests by using the 0.06 M solution, indeed the catalyst deactivates during tests with concentrated gas mixtures. Furthermore, it is noteworthy that the activation with TOS under the two initial reaction conditions takes place for Rh5-c900-0.06 M, suggesting a similar Rh speciation regardless of the total metal concentration.

The characterisation of the Rh5-c900-0.06 M sample after catalytic tests evidences film modifications similar to those above reported for Rh5-c900. While Mg-rich layers are stable and almost crack-free, the detachment of the Rh and Al-rich outer layer continues during catalytic tests. A particle size distribution in the 10–80 nm range is measured in the used sample with a 24 nm mean value (Fig. 11a). The largest Rh⁰ particles are usually present in the thickest layers (Fig. 11c), while small and well distributed particles locate in the film in close contact with the metallic support and in the middle of the Al₂O₃ needles (Fig. 11b). The latter Rh⁰ particles suggest that the needles are not only related to Al₂O₃ formed by oxidation of the FeCrAlloy support, but to an electrodeposited Al₂O₃ or MgAl₂O₄.

Hence, in the Rh5-c900-0.06 M catalyst a higher amount of dispersed Rh particles in a thicker and more homogeneous coating layer, in comparison with Rh5-c900 sample, improves the performances; although the deactivation by feeding concentrated gas mixtures cannot be avoided.

3.3. Bimetallic Rh/Ni catalyst

The inclusion of a second metal such as Ni in the catalyst formulation increases the number of active sites contributing to the conversion of CH₄. However, the electrosynthesis of a HT compound containing four different cations is highly challenging. The partial replacement of Mg²⁺ cations by Ni²⁺ ones in the electrolytic solution (Rh/Ni/Mg/Al = 5/15/55/25 a.r.) improves the coverage degree of the foam surface; the lower pH required to precipitate Ni than Mg-containing HT precursors may explain this behaviour [42]. Again several layers of solid are identified in SEM images, whose composition seems to be related with the precipitation pH of the individual hydroxides. The deposition of Mg and Ni is low in very thin layers, while the Mg/Ni a.r. is close to the expected one, 3.7, for intermediate thicknesses, and decreases to ca. 2.5–1.0 for thicker layers. Likewise in the above commented samples, Al and Rh contents are larger in the outer layer. After calcination (Fig. 12a), the same general trend previously commented for the Rh/Mg/Al samples is observed, although it appears that the film is more stable, i.e.

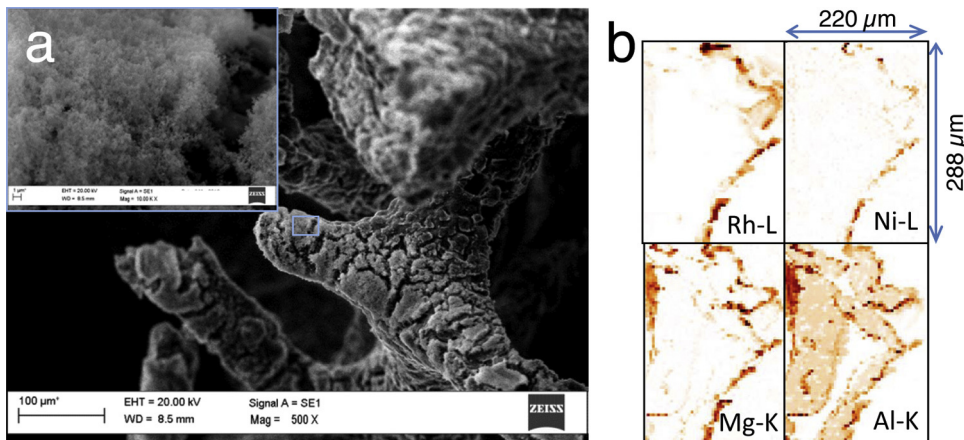


Fig. 12. Secondary SEM image (a) and elemental distribution maps recorded on a cross-section (b) of the bimetallic Rh5Ni-c900 catalyst.

the detachment of the film is less evident. The Ni and Rh contents are 7–15 and 3–15 wt.%, respectively.

Elemental XRF maps of some foam struts confirm that the distribution of Ni in the Rh5Ni-c900 catalyst correlates with those of Mg, Rh and Al (Fig. 12b). It is not possible to fit the spectra; but the Rh-L₃ edge (inflection points) suggests that there are no differences in the Rh speciation in comparison to the above commented Rh/Mg/Al samples.

On the other hand, the partial replacement of Mg by Ni largely improves the catalytic performances. The bimetallic Rh5Ni-c900 catalyst reaches conversion values around or above 90% in all the reaction conditions (Fig. 10), and consequently both the selectivity in CO and H₂ are above 95%. Despite the high activity, the catalyst steadily deactivates under both concentrated and diluted reaction conditions, mainly during the test at lowest GHSV, wherein a lower amount of heat is developed. The oxidation of nickel species may explain this behaviour, although the detachment of some parts of the coating, observed by SEM imaging, may be not be excluded. An electrosynthesised foam containing only Ni as active phase was not active [43], hence it may be stated that, similar to conventional pelletized samples, Rh helps to keep Ni in the reduced and consequently active state [55], although its oxidation or other type of deactivation cannot be fully avoided.

4. Conclusions

The tailoring of Rh content and concentration of metals in the electrolytic solution as well as the formation of bimetallic Rh/Ni particles lead to catalysts with smaller, more dispersed, and stabilised Rh⁰ particles in the coating, achieving a higher activity, although the stability should be still be improved.

The Rh content in the precipitated solid, present as hardly reducible Mg (Rh_{1-x}Al_x)₂O₄, correlates with the Rh loading in the solution; hence, Rh particle size decreases by modifying the Rh/Mg/Al ratio in the electrolytic solution from 11/70/19 to 5/70/25 and 2/70/28 a.r.% (0.03 M total concentration). However, the precipitation of a film enriched in Al and Rh (outer layer), after the deposition of a solid with a composition close to the expected one, generates differences in particle size and dispersion with the coating thickness. For these samples, the catalytic activity is mainly related to the Rh content rather than to the metallic particle size, and Rh species suffer from reduction and oxidation with TOS depending on the dilution degree of the CH₄/O₂/He reaction gas mixture.

The total metal concentration is the main parameter to be modified to precipitate thick films with a high amount of active sites, but without altering the growth and sintering behaviour of Rh⁰ particles and, therefore, achieving a better activity. While the addition of Ni to the electrolytic solution contributed to the catalytic activity but the catalyst steadily deactivates.

Further improvements are required to control the composition of the deposited solid, which determines not only the metallic particle size, but also the adhesion of the film during calcination and catalytic tests.

Acknowledgements

The Authors acknowledge M. Salome for helping during the μ XRF/XANES experiments at ID21 Beamline of the ESRF, the Department of Structural Characterisation of CNR-IMM of Bologna for the access to the FEG-SEM facility and Dr F. Ospitali for the scientific support. Thanks are due to Farrel Lytle database for providing the necessary Rh metal spectrum (rhfoil.a99 in http://ixs.iit.edu/data/Farrel_Lytle_data/). The financial support from the Ministero

per l'Istruzione, l'Università e la Ricerca (MIUR, Roma, Italy) and the University of Bologna (FARB program) is gratefully acknowledged.

Appendix A. Supplementary data

Supplementary data associated with this article can be found, in the online version, at <http://dx.doi.org/10.1016/j.apcatb.2015.05.035>

References

- [1] L.E. Basini, A. Guarinoni, Ind. Eng. Chem. Res. 52 (2013) 17023–17037.
- [2] B. Enger, R. Lødeng, A. Holmen, Appl. Catal. A 346 (2008) 1–27.
- [3] R. Horn, K.A. Williams, N.J. Degenstein, A. Bitsch-Larsen, D. Dalle Nogare, S.A. Tupy, L.D. Schmidt, J. Catal. 249 (2007) 380–393.
- [4] D. Dalle Nogare, N.J. Degenstein, R. Horn, P. Canu, L.D. Schmidt, J. Catal. 258 (2008) 131–142.
- [5] A. Donazzi, M. Maestri, B.C. Michel, A. Beretta, P. Forzatti, G. Groppi, E. Tronconi, L.D. Schmidt, D.G. Vlachos, J. Catal. 275 (2010) 270–279.
- [6] M. Maestri, D. Livio, A. Beretta, G. Groppi, Ind. Eng. Chem. Res. 53 (2014) 10914–10928.
- [7] C.T. Goralski Jr., R.P. O'Connor, L.D. Schmidt, Chem. Eng. Sci. 55 (2000) 1357–1370.
- [8] I. Tavazzi, A. Beretta, G. Groppi, M. Maestri, E. Tronconi, P. Forzatti, Catal. Today 129 (2007) 372–379.
- [9] A. Beretta, G. Groppi, M. Lualdi, I. Tavazzi, P. Forzatti, Ind. Eng. Chem. Res. 48 (2009) 3825–3836.
- [10] E. Tronconi, G. Groppi, C. Visconti, Curr. Opin. Chem. Eng. 5 (2014) 55–67.
- [11] K. Liu, G.D. Deluga, A. Bitsch-Larsen, L.D. Schmidt, L. Zhang, In Hydrogen and Syngas Production and Purification Technologies, in: K. Liu, C. Song, V. Subramani (Eds.), John Wiley & Sons, Inc., Hoboken, New Jersey, 2015, pp. 127–155.
- [12] T. Liu, C. Snyder, G. Veser, Ind. Eng. Chem. Res. 46 (2007) 9045–9052.
- [13] S. Cimino, L. Lisi, G. Russo, R. Torbati, Catal. Today 154 (2010) 283–292.
- [14] A. Donazzi, D. Livio, C. Diehm, A. Beretta, G. Groppi, P. Forzatti, Appl. Catal. A 469 (2014) 52–64.
- [15] O. Korup, C.F. Goldsmith, G. Weinberg, M. Geske, T. Kandemir, R. Schlögl, R. Horn, J. Catal. 297 (2013) 1–16.
- [16] A. Donazzi, B.C. Michael, L.D. Schmidt, J. Catal. 260 (2008) 270–275.
- [17] G. Landi, P.S. Barbato, S. Cimino, L. Lisi, G. Russo, Catal. Today 155 (2010) 27–34.
- [18] L. Coleman, E. Croiset, W. Epling, M. Fowler, R. Hudgins, Catal. Lett. 128 (2009) 144–153.
- [19] S. Cimino, L. Lisi, G. Mancino, M. Musiani, L. Vázquez-Gómez, E. Verlato, Int. J. Hydrogen Energy 37 (2012) 17040–17051.
- [20] H. Jung, W.L. Yoon, H. Lee, J.S. Park, J.S. Shin, H. Lab, J.D. Lee, J. Power Sources 124 (2003) 76–80.
- [21] A. Shamsi, J.J. Spivey, Ind. Eng. Chem. Res. 44 (2005) 7298–7305.
- [22] L. Bobrova, N. Vernikovskaya, V. Sadykov, Catal. Today 144 (2009) 185–200.
- [23] E. Verlato, S. Barison, S. Cimino, F. Dergal, L. Lisi, G. Mancino, M. Musiani, L. Vázquez-Gómez, Int. J. Hydrogen Energy 39 (2014) 11473–11485.
- [24] K.I. Hohn, L.D. Schmidt, Appl. Catal. A 211 (2001) 53–68.
- [25] M. Maestri, A. Beretta, G. Groppi, E. Tronconi, P. Forzatti, Catal. Today 105 (2005) 709–717.
- [26] A. Beretta, A. Donazzi, D. Livio, M. Maestri, G. Groppi, E. Tronconi, P. Forzatti, Catal. Today 171 (2011) 79–83.
- [27] T. Maffei, S. Rebughini, G. Gentile, S. Lipp, A. Cuoci, M. Maestri, Chem. Ing. Tech. 86 (2014) 1099–1106.
- [28] D. Livio, A. Donazzi, A. Beretta, G. Groppi, P. Forzatti, Top Catal. 54 (2011) 866–872.
- [29] J.E.P. Navalho, I. Frenzel, A. Loukou, J.M.C. Pereira, D. Trimis, J.C.F. Pereira, Int. J. Hydrogen Energy 38 (2013) 6989–7006.
- [30] S. Ding, Y. Yang, Y. Jin, Y. Cheng, Ind. Eng. Chem. Res. 48 (2009) 2878–2885.
- [31] S. Cimino, G. Landi, L. Lisi, G. Russo, Catal. Today 105 (2005) 718–723.
- [32] C.J. Bell, C.A. Leclerc, Energy Fuels 21 (2007) 3548–3554.
- [33] A.S. Bodke, S.S. Bharadwaj, L.D. Schmidt, J. Catal. 179 (1998) 138–149.
- [34] M.J. Stutz, D. Poulikakos, Chem. Eng. Sci. 63 (2008) 1761–1770.
- [35] V. Meille, Appl. Catal. A 315 (2006) 1–17.
- [36] A. Montebelli, C.G. Visconti, G. Groppi, E. Tronconi, C. Cristiani, C. Ferreira, S. Kohler, Catal. Sci. Technol. 4 (2014) 2846–2870.
- [37] U. Zavyalova, F. Girsdis, O. Korup, R. Horn, R. Schlögl, J. Phys. Chem. C 113 (2009) 17493–17501.
- [38] A. Donazzi, D. Pagani, A. Lucotti, M. Tommasini, A. Beretta, G. Groppi, C. Castiglioni, P. Forzatti, Appl. Catal. A 474 (2014) 149–158.
- [39] R. Chakrabarti, J.S. Kruger, R.J. Hermann, S.D. Blass, L.D. Schmidt, Appl. Catal. A 483 (2014) 97–102.
- [40] J.-D. Grunwaldt, S. Hannemann, C.G. Schroer, A. Baiker, J. Phys. Chem. B 110 (2006) 8674–8680.
- [41] F. Basile, P. Benito, G. Fornasari, A. Vaccari, Appl. Clay Sci. 48 (2010) 250–259.
- [42] P. Benito, F. Basile, G. Fornasari, M. Monti, E. Scavetta, D. Tonelli, A. Vaccari, In New Strategies in Chemical Synthesis and Catalysis, in: B. Pignataro (Ed.), Wiley-VCH, Weinheim, Germany, 2012, pp. 201–217, Chapter 6.

- [43] F. Basile, P. Benito, G. Fornasari, M. Monti, E. Scavetta, D. Tonelli, A. Vaccari, *Stud. Surf. Sci. Catal.* 175 (2010) 51–58.
- [44] F. Basile, P. Benito, G. Fornasari, M. Monti, E. Scavetta, D. Tonelli, A. Vaccari, *Catal. Today* 157 (2010) 183–190.
- [45] P. Benito, M. Monti, I. Bersani, F. Basile, G. Fornasari, E. Scavetta, D. Tonelli, A. Vaccari, *Catal. Today* 197 (2012) 162–169.
- [46] M. Monti, P. Benito, F. Basile, G. Fornasari, M. Gazzano, E. Scavetta, D. Tonelli, A. Vaccari, *Electrochim. Acta* 108 (2013) 596–604.
- [47] P. Benito, W. de Nolf, G. Nuyts, M. Monti, G. Fornasari, F. Basile, K. Janssens, F. Ospitali, E. Scavetta, D. Tonelli, A. Vaccari, *ACS Catal.* 4 (2014) 3779–3790.
- [48] P. Benito, M. Monti, W. De Nolf, G. Nuyts, G. Janssen, G. Fornasari, E. Scavetta, F. Basile, K. Janssens, F. Ospitali, D. Tonelli, A. Vaccari, *Catal. Today* 246 (2015) 154–164.
- [49] G.H.A. Therese, P.V. Kamath, *Chem. Mater.* 12 (2000) 1195–1204.
- [50] M. Nobial, O. Devos, O.R. Mattos, B. Tribollet, *J. Electroanal. Chem.* 600 (2007) 87–94.
- [51] I. Reyero, I. Velasco, O. Sanz, M. Montes, G. Arzamendia, L.M. Gandía, *Catal. Today* 216 (2013) 211–219.
- [52] I. Zhitomirsky, *Adv. Colloid Interface Sci.* 97 (2002) 279–317.
- [53] G.H.A. Therese, P.V. Kamath, *Chem. Mater.* 11 (1999) 3561–3564.
- [54] M. Dinamani, P.V. Kamath, *J. Appl. Electrochem.* 34 (2004) 899–902.
- [55] F. Basile, G. Fornasari, F. Trifirò, A. Vaccari, *Catal. Today* 64 (2001) 21–30.
- [56] M. Salome, M. Cotte, R. Baker, R. Barrett, N. Benseny-Cases, G. Berruyer, D. Bugnazet, H. Castillo-Michel, C. Cornu, B. Fayard, R. Gagliardini, E. az nd Hino, J. Morse, E. Papillon, E. Pouyet, C. Rivard, V.A. Sole, J. Susini, G. Veronesi, 11th International Conference on Synchrotron Radiation Instrumentation (SRI 2012), Dirac House, Temple Back, Bristol BS1 6BE, England, 2013.
- [57] W.H. McMaster, N.K. Del Grande, J.H., Mallett, J.H. Hubbell, *Compilation of X-ray Cross Sections*, Lawrence Radiation Laboratory UCRL- 50174sec II, Rev. 1 (1969).
- [58] B. Ravel, M. Newville, *J. Synchrotron Radiat.* 12 (2005) 537–541.
- [59] V.A. Sole, E. Papillon, M. Cotte, P. Walter, J. Susini, *Spectrochim. Acta Part B* 62 (2007) 63–68.
- [60] A. Ballarini, P. Benito, G. Fornasari, O. Scelza, A. Vaccari, *Int. J. Hydrogen Energy* 38 (2013) 15128–15139.
- [61] G. Fiquet, P. Richet, G. Montagnac, *Phys. Chem. Miner.* 27 (1999) 103–111.
- [62] T.K. Sham, *Phys. Rev. B* 31 (1985) 1888–1902.
- [63] F.M.F. de Groot, Z.W. Hu, M.F. Lopez, G. Kaindl, F. Guillot, M. Trone, *J. Chem. Phys.* 101 (1994) 6570–6576.
- [64] K.-i. Shimizu, T. Oda, Y. Sakamoto, Y. Kamiya, H. Yoshida, A. Satsuma, *Appl. Catal.* 111–112 (2012) 509–514.
- [65] A.J. Bard, In *Electrochemical Methods: Fundamentals and Applications*, in: L.R. Faulkner (Ed.), 2nd Edition, 2001, pp. 137–155, Chapter 4.
- [66] Y. Hamlaoui, F. Pedraza, C. Remazeilles, S. Cohendoz, C. Rébéré, L. Tifouti, J. Creus, *Mater. Chem. Phys.* 113 (2009) 650–657.